An investigation on the ionospheric response to the volcanic explosion at Hunga Ha'apai in 2021

Shican Qiu[1]*, Zhanming Zhang[1,2], Willie Soon[3,4], Victor Manuel Velasco Herrera[5], Xiankang Dou[2]*

[1] Department of Geophysics, College of the Geology Engineering and Geomatics, Chang'an University, Xi'an, 710054, China

[2] School of Earth and Space Sciences, University of Science and Technology of China, Hefei, 230026, China

[3] Center for Environmental Research and Earth Sciences (CERES), Salem, MA 01970, USA

[4] Institute of Earth Physics and Space Science (ELKH EPSS), 9400, Sopron, Hungary.

[5] Instituto De Geofísica, Universidad Nacional Autónoma De México, Mexico City, Mexico

Corresponding author: Shican Qiu (scq@ustc.edu.cn) and Xiankang Dou (dou@ustc.edu.cn)

Key Points:

- The ionospheric TEC decayed starting 10 days before the main eruption and showed obvious fluctuations during the eruption phase.
- The anomaly propagated with autocorrelation-analyzed period of ~16.5 and ~8 hours during intermittent and main outbreak phases, respectively.
- The anomaly propagation is mainly expressed by low frequencies, with energy concentrated in the range of $0 - 10^{-3}$Hz.

Abstract

The Honga Ha'apai volcano eruption (20.536°S, 175.382°W in Tonga), which started intermittently around December 2021 and most violently erupted on January 15, 2022, is considered to be the largest volcanic outbreak in recent decades. In this research, we derived the ionospheric Total Electron Content (TEC) over Sanya (18.400°N, 109.600°E), Wuhan (30.530°N, 114.610°E), and Mohe (53.500°N, 122.370°E), from the Global Navigation Satellite System (GNSS) observations. Then we investigated the coupling between the volcano eruption and ionosphere through the TEC variations. The TEC anomaly decayed from 10 days before main eruption of the Honga Ha'apai volcano, and showed obvious fluctuations during the eruption phase. The TEC anomaly propagated periodically, with its autocorrelation-analysed period of about 16.5 hours during the intermittent outbreak and about 8 hours during the main outbreak phase. Its wavelet–analysed period is about 9.4 hours during the intermittent outbreak and about 9.4 hours and 18.8 hours during the main outbreak phase. The propagation is mainly expressed in low frequencies, with energy concentrated in the range of $0 - 10^{-3}$Hz. This study highlights that the pre-eruption activities may play an important role in the coupling between the volcanic eruption and ionosphere disturbances.

Key words: volcano eruption, Tonga, Honga Ha'apai, GNSS, TEC, ionosphere

Plain Language Summary

In this research, we study the response of ionosphere to the volcanic explosion of Honga Ha'apai through the Total Electron Content (TEC) over Sanya (18.400°N, 109.600°E), Wuhan (30.530°N, 114.610°E), and Mohe (53.500°N, 122.370°E), from the Global Navigation Satellite System (GNSS). We investigated the coupling between the volcano eruption and ionosphere through the TEC variations. We found that the TEC anomalies are propagated periodically with periods of about 8–9 hours and 16–19 hours during the intermittent activity phase and the main eruptive phase, respectively. We envision that these signals probably reflect the nature of the Honga Ha'apai volcano eruption processes.

1 Introduction

The Global Navigation Satellite System (GNSS) was first used for high–precision global position monitoring as early as the late 1970s [*Blewitt*, 1990; *Dong & Bock*, 1989]. The Chinese Meridian Project supports GNSS observations over different latitudes [*Meridian*, 2022; *Wang & Wei*, 2007]. The ionospheric Total Electron Content (TEC) can be calculated from the GNSS ground–based observational data. The TEC is one of the important physical parameters reflecting the temporal and spatial characteristics of the ionosphere. It is widely used in the studies of ionospheric disturbance term correction, ionospheric variation monitoring, and even long–distance emergency communication [*Blagoveshchensky et al.*, 2005; *Blewitt*, 1990]. The TEC is often affected by space weather (e.g., coronal mass injection (CME), solar proton event (SPE), etc.), geological activities (e.g., earthquakes, tsunamis, volcanic eruptions, etc.) and human activities (e.g., artificial explosions, large–scale radio communications, ionospheric heating, etc.) [*Cahyadi et al.*, 2021]. Recent studies have indeed shown and confirm that solid earth activity could directly or indirectly affect the ionosphere [*Verhulst et al.*, 2022; *Ricardo Garza-Girón et al.*, 2023].

Over the past 5 decades, more and more areas near earthquake zones and volcanic swarms have been gradually developed as the acceleration of global urbanization and population growth continues, leading to increase risks for human beings [*Unisdr*, 2015]. Many studies have pointed out that, in addition to obvious geological activities such as volcanic eruptions and seismic fractures, geological events will be accompanied by distinct electromagnetic and optical signals within the ionosphere [*Lockner*, 1983; *Freund*, 2000; *Gokhberg & Morgounov*, 1982; *Leonard & Barnes*, 1965]. Therefore, the coupling between geological activity and ionosphere has gradually been widely studied and focused on. In 1965, a 10–minute seismic–ionospheric coupling anomaly was discovered for the first time, suggesting a possible correlation between earthquakes and ionospheric disturbances [*Leonard & Barnes*, 1965]. This coupling relationship is subsequently determined to have occurred before the actual occurrence of geological activities and events [*Gokhberg & Morgounov*, 1982; *Minster*, 1994; *Larkina*, 1983]. In 1982, the pre–earthquake electromagnetic radiation outburst was first observed by the magnetometer on the OGO–6 satellite of the United States [*Gokhberg & Morgounov*, 1982]. In 1983, the very low frequency (VHF) wave was observed to be enhanced several minutes before and hours after an earthquake event, through the Intercosmos–19 satellite [*Larkina*, 1983]. In particular, such coupling was also found between the earthquake and the TEC variations. In the study of the Northridge earthquake in 1994, it was detected that the ionospheric GPS–TEC had related disturbances before and after the earthquake [*Minster*, 1994].

Nowadays, more and more studies have confirmed that the ionosphere can be effectively monitored in order to study the geological activities, through the method of combining satellites–borne data with traditional ground–based observations [*Cahyadi et al.*, 2022; *Cussac et al.*, 2006; *Liu*, 2004; *Liu et al.*, 2011; *Satti et al.*, 2022; *Zhang*, 2008; *Zhang et al.*, 2009]. Indeed, it is possible to obtain and study the variation pattern of geological activity during the whole period, that is, from the precursor to the later stage, based on the analyses of ionospheric parameters [*Liu*, 2004; *Kon et al.*, 2011; *Liu et al.*, 2006a; *Liu et al.*, 2000; *Liu et al.*, 2006b; *Satti et al.*, 2022; *Zhang*, 2008; *Zhang et al.*, 2009]. The TEC and the F2 layer critical frequency (f_0F_2) have been comfirmed as important indicators in the geological activity–ionosphere coupling [*Astafyeva et al.*, 2011; *Cahyadi et al.*, 2022; *Liu*, 2004; *Liu, & Liu*, 2011; *Liu et al.*, 2011; *Liu et al.*, 2006a; *Liu et al.*, 2006b; *Maletckii & Astafyeva*, 2022; *Parrot* et al., 2006a; *Parrot et al.*, 2006b; *Pulinets*, 2004; *Toman et al.*, 2021; *Zhang et al.*, 2009]. In addition, more detailed information, such as earthquake location, intensity, and local tectonic orientation, can be determined from the propagation pattern of the ionospheric disturbances [*Cahyadi et al.*, 2021; *Cahyadi et al.*, 2022; *Afraimovich*, 2001; *Le et al.*, 2011; *Liu et al.*, 2006a; *Liu et al.*, 2000]. The mechanism for this coupling has been analyzed, and candidates such as the ionizing radiation model and conductivity model have been proposed [*Lockner*, 1983; *Gokhberg & Morgounov*, 1985; *Parrot et al.*, 2006a; *Parrot et al.*, 2006b; *Pulinets*, 2004; *Zhang*, 2008]. Recently, Velasco Herrera et al. (2022) has reviewed the earthquake–ionosphere relationship as potential precursors for forecasting major strong earthquakes over major fault zones/regions of the world.

As for the specific direction of volcano–ionosphere coupling research, it has been established that there is a correlation between ionospheric and volcanic activity, with TEC variation as an effective diagnostic parameter [*Aoyama et al.*, 2016; *Cahyadi et al.*, 2021; *Cahyadi et al.*, 2020; *Heki & Fujimoto*, 2022; *Li et al.*, 2016; *Lin*, 2017; *Liu et al.*, 2017; *Maletckii & Astafyeva*, 2022; *Manta et al.*, 2021; *Pandara et al.*, 2021; *Saito*, 2022; *Shults et al.*, 2016; *Toman et al.*, 2021; *Verhulst et al.*, 2022; *Zhang et al.*, 2022]. Meanwhile, observation from multiple independent instruments can show more details and bring a fuller picture about the nature of the coupling [*Verhulst et al.*, 2022]. Thus, a combination observational data from both ground–based and space–based method is particularly important [*Heki & Fujimoto*, 2022; *Matoza et al.*, 2022; *Wright et al.*, 2022]. The combined analyses had found abnormal propagation that has multiple wave characteristics such as acoustic wave, infrasonic wave, ultrasonic wave and gravity wave, and periodic harmonic oscillation exists in volcanic eruptions [*Amores et al.*, 2022; *Aoyama et al.*, 2016; *Cahyadi et al.*, 2021; *Heki & Fujimoto*, 2022; *Lin*, 2017; *Lin et al.*, 2022; *Liu et al.*, 2022; *Liu et al.*, 2017; *Manta et al.*, 2021; *Nakashima et al.*, 2016; *Pandara et al.*, 2021; *Maletckii & Astafyeva*, 2022; *Matoza et al.*, 2022; *Ricardo Garza-Girón*, 2023; *Shults et al.*, 2016; *Kubota et al.*, 2022; *Toman et al.*, 2021; *Verhulst et al.*, 2022; *Watson et al.*, 2022; *Wright et al.*, 2022; *Zhang et al.*, 2022]. By analyzing the spectrum of ionospheric anomalies, different wave propagation characteristics and volcanic eruption types can be distinguished [*Heki & Fujimoto*, 2022; *Li et al.*, 2016; *Liu et al.*, 2017; *Nakashima et al.*, 2016]. In addition, the intensity of ionospheric anomalies has also been confirmed to be significantly correlated with volcanic eruption intensity and plume height [*Cahyadi et al.*, 2020; *Manta et al.*, nbo; *Shults et al.*, 2016; *Toman et al.*, 2021]. Based on the study of anomalous propagation characteristics in the ionosphere, a variety of information can be obtained, including the location of volcanic source, the scale of volcanic eruption, the height of plume, the rate of material ejection and the quality of ejection materials [*Cahyadi et al.*, 2020; *Li et al.*, 2016; *Maletckii & Astafyeva*, 2022; *Shults et al.*, 2016; *Watson et al.*, 2022]. In the study of volcanic eruption activity cycles, it has been found that ionospheric anomalies can occur several days before the main eruption event [*Li et al.*, 2016; *Pandara et al.*, 2021; *Toman et al.*, 2021]. Particularly, the enhancement of TEC has been observed to occur during the main phase of volcanic eruption [*Toman et al.*, 2021].

Overall, the specific physical mechanism of volcanic–ionosphere coupling is still highly uncertain, which is why a large number of observational evidence is both necessary and important [*Lockner*, 1983; *Gokhberg & Morgounov*, 1985; *Parrot et al.*, 2006a; *Parrot et al.*, 2006b; *Pulinets*, 2004; *Zhang*, 2008]. For our case study, we consider the Hunga Ha'apai volcanic eruption in Tonga (20.536°S, 175.382°W), which is one of the strongest volcanic eruptions in recent years with a start date on December 20, 2021 universal time (UT) [*Poli & Shapiro*, 2022; *Matoza et al.*, 2022]. After the first eruption, vocanic activities continued to come and go but weaken for about two weeks [*INGV*, 2022; *Kusky*, 2022; *NPR*, 2022]. After that, the eruption resumed on January 13, 2022, and the largest outbreak was observed at around 4:00 UT on January 15 when the top umbra cloud reached a maximum diameter of 500 km [*GVP*, 2022; *INGV*, 2022; *Kusky*, 2022; *NASA*, 2022; *NPR*, 2022]. Current analysis suggests that it has a Volcanic Explosivity Index (VEI) of 5 or 6 or even higher [*INGV*, 2022; *NASA*, 2022; *Poli & Shapiro*, 2022]. Proud et al. (2022) recently confirmed that the volcanic cloud for this event reached the extreme height of 57 km at its highest extent.

The main purpose of this study is to investigate the coupling between volcanic eruption and the ionosphere. The vertical TEC is used as the indicator of ionospheric disturbance, through the ground–based GNSS observations over Sanya, Wuhan, and Mohe stations, of the Chinese Meridian Project. The Tonga volcanic eruption is divided into two stages: the first stage is mostly with intermittent eruption activities, lasting about two weeks since December 20, 2021 and then weakened around January 3; the second stage is the main outbreak phase, starting on January 13 with a large–scale concentrated eruption persisting for many consecutive days. This study can offer as a supplementary method to tackle certain cases of eruptions when there are significant data gaps or simply with missing data.

2 Data and Method

In this study, the ground–based GNSS observational data, the Broadcast Ephemeris Products, the Differential Code Biases data (DCB) between the satellite and ground station, and the volcanic eruption development data are processed.

Based on the GNSS data, the TEC can be estimated using the ionospheric delay term. According to the theory, the propagation velocity of the ranging code in the ionosphere is the group velocity V_g, from which the geometric distance ρ between the satellite and the ground receiver satisfies the following equation:

$$\rho = \int_{\Delta t} V_g dt = \int_{\Delta t} (\mathrm{c} - 40.28\mathrm{c}\frac{N_e}{f^2}) dt = c\Delta t - \frac{40.28}{f^2}\int_{\Delta t} \mathrm{c} N_e dt \, , \quad (1)$$

where Δt is the propagation time of satellite signal passing to the ground receiver [*Feng*, 2020].

The signal path through the ionosphere can be approximated by a cylinder–shaped volumetric tube, the TEC expression can be obtained from the definition as:

$$TEC = \int N_e ds \, , \quad (2)$$

Then the delay magnitude for ionospheric effects on phase (I_P) and ranging code (I_g) can be expressed as follows:

$$I_P = -I_g = \frac{40.28}{f^2} TEC, \tag{3}$$

In the dual–frequency GNSS system, there will be clock offsets, multi–path delays, hardware delays, and observational noises. Therefore, the following equations are used for the calculation:

$$TEC_P = \alpha P = \alpha(P_1 - P_2) = TEC_{abs} + DCB, \tag{4}$$

$$TEC_L = \alpha L = \alpha(L_1 - L_2) = TEC_{abs} + DCB + \frac{1}{\alpha}(\lambda_1 N_1 - \lambda_2 N_2), \tag{5}$$

$$L_1 = \lambda_1 \phi_1, \tag{6}$$

$$L_2 = \lambda_2 \phi_2, \tag{7}$$

where

TEC_P ~ differential pseudorange TEC, also known as absolute TEC;

P_1 and P_2 ~ pseudorange of the dual–frequency observations;

TEC_{abs} ~ true value of TEC;

DCB ~ differential code deviation;

TEC_L ~ carrier phase TEC, also known as relative TEC;

λ_1 and λ_2 ~ the wavelengths of phase carriers L_1 and L_2, respectively;

N_1 and N_1 ~ the whole–period ambiguities of phase carriers L_1 and L_2, respectively;

and

ϕ_1 and ϕ_2 ~ the carrier phase [*Feng*, 2020].

Base on the calculations of TEC, a comparison of TEC for each day with the median value for that period can be obtained. Then Fourier and autocorrelation analyses are carried out for examining the abnormal variation of TEC. The Fast Fourier Transform (FFT) is performed as

$$X_m = \sum_{n=0}^{N-1} x_n e^{-inm\frac{2\pi}{N}} \quad (0 \le m \le N-1), \tag{8}$$

$$\begin{cases} X_l = G_l + W_N^l H_l \\ X_{\frac{N}{2}+l} = G_l - W_N^l H_l \end{cases} \quad \left(0 \le l \le \frac{N}{2} - 1\right), \tag{9}$$

where

X_m ~ the finite discrete spectrum;

x_n ~ the finite discrete signal;

G_l and H_l ~ the discrete spectra of the even and odd terms, respectively;

and

$$W_N^l = e^{-i\frac{2\pi}{N}} \text{ [\textit{Cheng}, 2010].}$$

When the calculation is simplified to only one term, its finite discrete spectrum is the finite discrete signal itself, and the inverse derivation can be performed. The autocorrelation function is calculated using the following equation

$$r_{xx}(\tau) = \sum_{n=-\infty}^{\infty} x_n \, x_{n-\tau} = x_n * x_{-n}, \tag{10}$$

where $r_{xx}(\tau)$ is the autocorrelation function with respect to the time shift τ and x_n is the calculated signal [*Cheng*, 2010].

As shown in Eq. (10), the signal amplitude will gradually deviate from the corresponding value with the time shift, resulting in the reduction of the amplitude of the correlation function. However, when the signal has quasi–periodicity, it will reveal an approximately equally spaced amplitude. The amplitude attenuation from the correlation results will be weakened, and there will appear obvious sub–peaks that are slightly smaller than the main peak. The number of subpeaks is related to the number of original peaks in the calculated signal, and can be inferred from the correlation function.

3 Ionospheric Response to Volcanic Eruption

In this study, we speculate or assume that the pre-eruption phase will cause dense earthquakes and release significant amounts of gas from magma capsule as the Figure 1 below sketched. These processes will change the composition over local atmosphere and generate both gravity and seismic waves, and hence will further affect the ionosphere [*Sigurdsson et al.*, 2015]. We believe that there are a variety of gases dissolved in magma capsule like carbon dioxide (CO_2), sulfur dioxide (SO_2), hydrogen sulfide (H_2S), carbon monoxide (CO), hydrogen chloride (HCl) and so on [*Sigurdsson et al.*, 2015]. There are sufficient evidence to suggest that these gases which leak from underground fissure during the pre–eruption period can change the temperature of upper atmosphere and lower the electron density [*Cnossen*, 2022; *Qian et al.*, 2013; *Roble & Dickinson*, 1989]. In the meantime, during the peak phase of volcanic eruptions much more gravity wave, seismic wave, acoustic wave and infrasonic wave will be generated [*Ricardo Garza-Girón*, 2023]. Although this effect is not global and have low strength, the local variation will propagate outward by the dynamic action of the upper atmosphere.

The data for the first stage (from December 10 to 31, 2021) are shown in Figure 2(a–l). The horizontal coordinate is Day of year (Doy) and the ordinate is Total Electron Content Unit (TECU), where 1 TECU means 10^{16} electrons per unit area. It can be observed that at the beginning of the December 20 (Doy354), the fitted values deviate obviously and significantly from the median. The TEC fluctuates significantly, and the largest peak value of TEC reaches 50 TECU, much higher than the average daily maximum of 20–30 TECU. Figure 2(m–t) exhibits the observed results from January 10 to 25, 2022. The data shows a disturbance on January 15, 2022 (Doy15), but the amplitude is distinctly smaller than that in Figure 2(a–l).

The variations of the anomaly values obtained by subtracting the observed TEC from the median are shown in Figure 3. Similar characteristics of the TEC anomalies occur over different stations. In the period before the formal eruptions for both stages, the TEC decays in different degrees. The attenuation amplitude in the intermittent stage is much larger, with obvious characteristics of oscillation and fluctuation after the outburst starts. Meanwhile, there are obvious differences between stations. According to the Space Environment Prediction Center (SEPC), there is a moderate geomagnetic storm occurred at January 14 and 15, which may induce ionospheric responses [*SEPC*, 2022a, 2022b]. The effect of a storm is wide and global with minimal attenuation between different stations. On the contrary, the anomalies caused by a volcanic eruption will decay with the propagation obviously, and have a distinct variation from quiet period and clear fluctuation characters. From Figure 3, we can find out that the intensity of anomaly decreases with the increase of distance to Honga Ha'apai. This is similar to previous study. According to Verhulst et al. (2022), they found that the TIDs during this period are not of auroral origin, i.e., not related to the geomagnetic storm [*Verhulst et al.*, 2022]. Therefore, we believe that the impact of the Honga Ha'apai eruption is much more prominent than that from the moderate magnetic storm.

Therefore, the TEC anomaly over Sanya station, which is closer to Tonga, is more intense compared to that of Wuhan and Mohe stations. But there are anomalous peaks in Wuhan and Mohe, which do not appear in Sanya. On December 20 (Doy354) and 21 (Doy355), distinct TEC enhancement occurs over Wuhan and Mohe, while the TEC oscillates obviously over Sanya on that time. On January 15 (Doy15) and 16 (Doy16), the fluctuation of TEC anomaly shows similar distinct waveform characteristics. If we consider the two maxima between Doy 15 and Doy 16 (pointed out by the blue asterisks in Figure 3b, 3d, and 3f), the calculated time difference is about 21.7 hours for Sanya, 19.9 hours for Wuhan, and 20.5 hours for Mohe, respectively. These two fluctuations may be generated by the same disturbance originated from the eruption, but they arrive at observed stations from two opposite directions over the globe. Based on the coordinates of Sanya station in Hainan (18.400°N, 109.600°E), Wuhan in Hubei (30.530°N, 114.610°E), Mohe in Heilongjiang (53.500°N, 122.370°E), and Honga Ha'apai volcano in Tonga (20.536°S,175.382°W), the time difference of the anomaly arriving at observed stations from two directions can be evaluated using the ellipsoid model of the Earth.

The Earth's ellipsoidal model is given as follows:

$$r = \sqrt{(x_2 - x_1)^2 + (y_2 - y_1)^2 + (z_2 - z_1)^2}, \tag{11}$$

$$S = r + \frac{r^3}{24*k^2} + \frac{3*r^5}{640*k^4}, \tag{12}$$

and the time difference can be calculated by

$$\Delta T = T_1 - T_2 = \frac{H - S}{v} - \frac{S}{v}, \tag{13}$$

where

(x_1, y_1, z_1) and (x_2, y_2, z_2) ~ the coordinate positions of the two points in the Cartesian coordinate system;

r ~ the straight–line distance between the two points;

S ~ the distance between the two points on the ellipsoid surface;

k ~ the curvature radius of the arc between the two points;

T_1 and T_2 ~ the time for the propagation from the two opposite directions;

v ~ the anomaly propagation velocity;

and H is the circumference of the Earth (e.g., $H = 2\pi R$, and R is the Earth radius).

Setting the Earth's eccentricity of about 0.082, the semi–major axis of the Earth's ellipsoid of 6378.137 km, the ionosphere height of 350 km, and v ranges $300 \sim 350\ km/s$ according to the recent reference, the calculated average time differences is $\Delta T_{Sanya} = 19.58 \pm 3.36$hours, $\Delta T_{Mohe} = 17.97 \pm 3.36$ hours and $\Delta T_{Wuhan} = 19.35 \pm 3.36$ hours, where the measured time differences is nearly within the calculated range.

4 Discussion

As seen in Figure 3, the fluctuation characteristics of the anomalies are consistent among different stations, but a certain degree of attenuation may occur at some stations. For analysis of the characteristics of the volcanic eruption signals, we make further processing on the anomalous signals to explore the coupling between the volcanic activities and ionospheric variations.

4.1 The Autocorrelation Analysis and Wavelet Analysis

The autocorrelation has little effect on the periodicity of the original signal, so the results can be used to analyze the periodicity of the anomalies in the first or initial stage of analysis. The autocorrelation of the TEC anomaly over Sanya during the intermittent stage is shown in Figure 4a, which reveals that the maximum peak is not prominent when compared to other smaller peaks. This result indicates that with time shift, the differences in TEC anomalies caused by each eruption are similar throughout stage 1. However, the interval of each volcanic eruption is not completely consistent, so in the process of calculating autocorrelation and continuous time shift, there will be a smaller peak similar to that with large correlation. Since the interval of each eruption is not completely consistent, smaller peaks similar to the larger correlations will occur in the process of calculating autocorrelation with continuous time shift.

As the time shift increases, it can be seen that the image is clearly divided into two regions, and the amplitude corresponding to the first 5000 points in the first half of the autocorrelation function is small overall. This is because the anomalous features in the precursor phase may differ significantly from those in the outbreak phase, and the correlation becomes worse as the time shift increases. And according to the principle of autocorrelation, there are about 4 or 5 sub–peaks in the correlation function results that are close to the main frequency peak. This indicates that there are also a number of correlated peaks in the original calculated signals, and these peaks are the regions where the TEC anomaly changes the most, so it can be tentatively judged that there were at least 3–4 outbursts of similar size to the December 20th's intermittent outburst stage.

In addition, as shown in Figure 4b, during the main eruption phase, the detected main peaks are 4–10 times larger than the neighboring smaller peaks over Sanya station. This result indicates that the eruption size in this stage is the largest and most concentrated during the violent eruption phase. Periodic analysis of the portion of the autocorrelation function with peaks greater than 10^4 and suggests the existence of a 16.5–hour periodic variation characteristic for stage 1 and an 8–hour periodic variation characteristic for stage 2.

Furthermore, Figure 4c (for Wuhan) and 4e (for Mohe) show similar results during the intermittent stage to Figure 4a. And in Figure 4d and 4f, we can find a similar pattern of autocorrelation results during the main eruption phase as in Figure 4b. However, the amplitude of the autocorrelation results for the Mohe and Wuhan become significantly reduced, with about one order of magnitude smaller than that of Sanya. This discrepancy indicates that the signal intensity is attenuated during the propagation.

On the other hand, the wavelet transform can perform high and low filtering and time-frequent domain analysis with higher resolution [*Chen et al.*, 2021; *Hubbard*, 1998; *Pan et al.*, 2008]. Therefore, more detailed information on the signals can be obtained by adopting wavelet analysis. With this property, the signal period can be extracted while at the same time the signal can be filtered according to the selected wavelet and scale. The result of wavelet analysis of the TEC anomaly during the intermittent stage is shown in Figure 5a. We can find that there is a periodic oscillation of 9.4 hours in the intermittent stage. In the results of the main eruption stage, we found the periodic variations of 9.4 hours and 18.8 hours (as shown in Figure 5b). The results of wavelet analysis shown in Figure 5 are basically consistent with those of autocorrelation analysis from Figure 4a and 4b.

4.2 The Fourier Analysis

From the wavelet transform results with the high frequency part, it can be observed that signals seldom concentrate in the high frequency regime (Figure 6a and 6b). Considering the volcanic activity is continuous in the selected time period, the low frequency part of the signal can be further analyzed by the Fourier analysis. Compared with wavelet transform, the Fourier transform is more suitable to deal with the whole signal. Based on these characteristics, the Fourier transform can be used to highlight frequency ranges where the signal energy is more concentrated [*Chen et al.*, 2021; *Iyer*, 1968; *Toman*, 1966; *Troyan & Kiselev*, 2010]. The Fourier analysis for the anomaly of TEC during the intermittent stage and the main eruption stage is performed, with the output amplitude spectra shown in Figure 6c and 6d. It can be confirmed from Figure 6c that the energy of the anomalous fluctuations during the intermittent stage is mainly concentrated in the frequency range of an order of $0-10^{-3}$Hz. Figure 6d shows the amplitude spectrum of the TEC anomalies during the main phase. The energy of the anomalous fluctuations during the main stage is also concentrated in the frequency range of an order of $0-10^{-3}$Hz. These results indicates that the anomalous fluctuations caused by the eruption are mainly low–frequency waves. However, the maximum amplitude of the wave of the main phase is smaller than that of the intermittent stage. Therefore, it is probably that some physicochemical processes occurring during the intermittent phase that have a greater effect on the energy of the fluctuations. The precursor in the early stage of the eruption has a greater impact on ionospheric disturbances, and the difference in precursory activities between stage 1 and stage 2 would possibly lead to the distinct fluctuations during the two stages.

4.3 Possible Coupling between the Volcanic Eruptions and TEC Variations

The analysis here reveals that the physicochemical processes at different stages of volcanic activity are distinct, indicating different mechanisms for their effects on the TEC variations. Figure 3 shows that in the precursory stage, the TEC exhibits a significant attenuation. For the Surtseyan and Plinian eruptions, during the precursor stage (as showing in Figure 1), large–scale escape of gases from the magma storage occurs, such deeply–rooted gases are released by crustal rupture, and underground materials sublimate fast. Therefore, the magma does not overflow at this precursor stage yet. During the main eruption stage, it is often accompanied by the eruption of lava, volcanic ashes, and pyroclastic flows. The TEC also exhibits different abnormal characteristics from the previous stage. The variations of TEC first show distinct decline and then there are enhancement and attenuation alternately. And the enhancement propagates with obvious periodicity.

In addition, in the comparative analysis of intermittent stage and main eruptions stage, the variation of the peak value of TEC anomaly is revealed. In the intermittent eruption stage, the maximum TEC anomaly can reach 50 TECU, and the magnitude of TEC appears to be elevated throughout this period. During the main eruption phase, the maximum TEC anomaly reaches 30–40 TECU, and the TEC, however, does not exhibit any positive correlation between its increased magnitude and the eruption intensity. These results can match our hypothesis and observation that the greater effect of early volcanic activity on TEC is mainly because of the escaping materials/gasses during the precursor period. The lower density and the faster emission rate of the early escape materials, a large amount of gasses has already been depleted during the intermittent eruption phase. Since there is already reduced amount of residual matter in the magma storage, it will probably cause a smaller effect on TEC during the main eruption phase.

5 Conclusion

From the analysis carried out in this paper, it can be confirmed that the high sensitivity of TEC in relation to different stages of volcanic eruption is of great significance for studying the mechanism of the coupling between volcanic activity and ionosphere. Based on the results from this study, the following conclusions can be drawn:

1. From 10 days before the main eruption, obvious attenuation appeared in the TEC profiles. During the main phase, the TEC anomaly alternated between attenuation and enhancement. And the anomaly showed fluctuations in both stages.

2. The anomaly propagated periodically, with its autocorrelation-analysed period of about 16.5 hours during the intermittent outbreak and about 8 hours during the main outbreak phase. Its corresponding wavelet-analysed period is about 9.4 hours during the intermittent outbreak and about 9.4 hours and 18.8 hours during the main outbreak phase.

3. The anomaly propagation is mainly dominated and expressed by low frequencies, with energy concentrated in the range of $0-10^{-3}$Hz.

4. The anomaly generated by the Honga Ha'apai eruption arrived successively at observed stations from two opposite directions, with average differences of about 19.58 hours (Sanya), 19.35 hours (Wuhan), 17.97 hours (Mohe). Based on actual GNSS-TEC observation, the differences during this eruption are about 21.7 hours (Sanya), 19.9 hours (Wuhan), 20.5 hours (Mohe).

5. During the precursor stage of the eruption, there were large imprints on the TEC, while the amplitude of TEC anomaly during the main eruption phase is much smaller. This indicates that activites in pre-eruption stage like gas releasing have a greater impact on TEC than activities such as explosion generated by the eruption. This discrepancy may be related to the physical and chemical processes generated by a large number of volatile substances before the main phase of the eruption. This result can provide more evidence for the study of the coupling process between volcanic activity and ionosphere.

6. According to the results of our autocorrelation analysis, at least another five to six eruptions might have occurred with similar size to the case on December 20 during the intermittent phase.

Open Research

The ground–based GNSS observations are available from the Space Environment Ground–based Integrated Monitoring Network of Chinese Meridian Project database (http://meridianproject.ac.cn/). The GNSS Broadcast Ephemeris Products are downloaded from the IGS Data Center of Wuhan University (http://www.igs.gnsswhu.cn/). The DCB data of GNSS observation system come from NASA's Crustal Dynamics Data Information System website (https://cddis.nasa.gov/index.html). The volcanic eruption data are mainly from the Smithsonian Institution's Global Register of Volcanic Activity (https://volcano.si.edu/). The Geomagnetic activity information come from the Space Environment Prediction Center (http://www.sepc.ac.cn/). The seismic information are mainly from the U.S. Geological Survey (https://earthquake.usgs.gov/).

Acknowledgments

This work is supported by the National Natural Science Foundation of China (NO. 41974178). We acknowledge the Chinese Meridian Project for the ground observation data of GNSS, the IGS Data Center of Wuhan University for the broadcast ephemeris data, the Crustal Dynamics Data Information System for the DCB data, the Global Volcanism Program of Smithsonian Institution for the volcanic information, the Space Environment Prediction Center for the Geomagnetic activity information and the U.S. Geological Survey for the seismic information.

References

Afraimovich, E. L., Perevalova, N. P., Plotnikov, A. V., and Uralov, A. M. (2001). The shock–acoustic waves generated by the earthquakes. *Annales Geophysicae*, *19*: 395–409. doi:10.5194/angeo–19–395–2001

Amores, A., Monserrat, S., Marcos, M., Argüeso, D., Villalonga, J., Jordà, G., and Gomis, D. (2022). Numerical Simulation of Atmospheric Lamb Waves Generated by the 2022 Hunga–Tonga Volcanic Eruption. *Geophysical Research Letters, 49*(6). doi:10.1029/2022gl098240

Aoyama, T., Iyemori, T., Nakanishi, K., Nishioka, M., Rosales, D., Veliz, O., and Safor, E. V. (2016). Localized field–aligned currents and 4–min TEC and ground magnetic oscillations during the 2015 eruption of Chile's Calbuco volcano. *Earth, Planets and Space, 68*(1). doi:10.1186/s40623–016–0523–0

Astafyeva, E., Lognonné, P., and Rolland, L. (2011). First ionospheric images of the seismic fault slip on the example of the Tohoku–oki earthquake. *Geophysical Research Letters, 38*(22), n/a–n/a. doi:10.1029/2011gl049623

Blagoveshchensky, D. V., Lester, M., Kornienko, V. A., Shagimuratov, I. I., Stocker, A. J., and Warrington, E. M. (2005). Observations by the CUTLASS radar, HF Doppler, oblique ionospheric sounding, and TEC from GPS during a magnetic storm. *Annales Geophysicae, 23*(5), 1697–1709. doi:10.5194/angeo–23–1697–2005

Blewitt, G. (1990). An automatic editing algorithm for GPS data. *Geophysical Research Letters, 17*(3), 199-202.

Cahyadi, M. N., Handoko, E. Y., Rahayu, R. W., and Heki, K. (2021). Comparison of volcanic explosions in Japan using impulsive ionospheric disturbances. *Earth, Planets and Space, 73*(1). doi:10.1186/s40623–021–01539–5

Cahyadi, M. N., Muslim, B., Pratomo, D. G., Anjasmara, I. M., Arisa, D., Rahayu, R. W., . . . Hariyanto, I. H., Jin, S., and Muafiry, I. N. (2022). Co–Seismic Ionospheric Disturbances Following the 2016 West Sumatra and 2018 Palu Earthquakes from GPS and GLONASS Measurements. *Remote Sensing, 14*(2), 401. doi:10.3390/rs14020401

Cahyadi, M. N., Rahayu, R. W., Heki, K., and Nakashima, Y. (2020). Harmonic ionospheric oscillation by the 2010 eruption of the Merapi volcano, Indonesia, and the relevance of its amplitude to the mass eruption rate. *Journal of Volcanology and Geothermal Research, 405*, 107047. doi:10.1016/j.jvolgeores.2020.107047

Calais, E., and Minster, J. B. (1994). GPS detection of ionospheric perturbations following the January 17, 1994, Northridge Earthquake. *Geophysical Research Letters*, *22*(9), 1045–1048.

Cheng, Q. S. (2010). *Digital Signal Processing. 2nd edition*: Peking University Press.

Chen, X., Chen, H., Fang, Y., & Hu, Y. (2021). High-Order Synchroextracting Time–Frequency Analysis and Its Application in Seismic Hydrocarbon Reservoir Identification: *IEEE Geoscience and Remote Sensing Letters, 18*(11), 2011-2015. doi:10.1109/lgrs.2020.3009259

Cnossen, I. (2022). A Realistic Projection of Climate Change in the Upper Atmosphere Into the 21st Century. *Geophysical Research Letters, 49*(19). doi:10.1029/2022gl100693

Cussac, T., Clair, M.–A., Pascale, U.–G., Buisson, F., Gerard, L.–B., Ledu, M., Elisabelar, C., Passot, X., . . . Rey, N. (2006). The Demeter microsatellite and ground segment. *Planetary and Space Science, 54*(5), 413–427. doi:10.1016/j.pss.2005.10.013

Dong, D.–N., and Bock, Y. (1989). Global Positioning System Network analysis with phase ambiguity resolution applied to crustal deformation studies in California. *Journal of Geophysical Research: Solid Earth, 94*(B4), 3949–3966. doi:10.1029/JB094iB04p03949

Feng, J. D. (2020). Analysis of Ionospheric Time–varying Characteristics and its Empirical Modeling Method. *Metallurgical Industry Press*, 1st edition, pages:167.

Freund, F. (2000). Time–resolved study of charge generation and propagation in igneous rocks. *Journal of Geophysical Research: Solid Earth, 105*(B5), 11001–11019. doi:10.1029/1999jb900423

Gokhberg, M. B. and Morgounov, V. A. (1982). Experimental Measurement of Electromagnetic Emissions Possibly Related to Earthquakes in Japan. *Journal of Geophysical Research*. *87*(B9), 7824–7828.

Gokhberg, M. B. Gufeld, I. L., Gershenzon, N. I., and Pilipenko, V. A. (1985). Electromagnetic effects during rupture of the Earth's Crust, *Earth Physics*, *21*(1), 52–63.

GVP, S. I. (2022). Hunga Tonga–Hunga Ha'apai. Retrieved from https://volcano.si.edu/volcano.cfm?vn=243040

Heki, K., and Fujimoto, T. (2022). Atmospheric modes excited by the 2021 August eruption of the Fukutoku–Okanoba volcano, Izu–Bonin Arc, observed as harmonic TEC oscillations by QZSS. *Earth, Planets and Space, 74*(1). doi:10.1186/s40623–022–01587–5

Hubbard, B. B. (1998). The World According to Wavelets.*A. K. Peters ltd.*

INGV. (2022). La grande eruzione del vulcano Hunga Tonga – Hunga Ha'apai. Retrieved from https://ingvvulcani.com/2022/01/17/grande–eruzione–vulcano–hunga–tonga–hunga–haapai/

Iyer, H. M. (1968). Determination of Frequency-Wave-Number Spectra Using Seismic Arrays. *GEOPHYSICAL JOURNAL OF THE ROYAL ASTRONOMICAL SOCIETY, 16*, 97-117.

Kon, S., Nishihashi, M., and Hattori, K. (2011). Ionospheric anomalies possibly associated with M⩾6.0 earthquakes in the Japan area during 1998–2010: Case studies and statistical study. *Journal of Asian Earth Sciences, 41*(4–5), 410–420. doi:10.1016/j.jseaes.2010.10.005

Kubota, T., Saito, T., and Nishida, K. (2022). Global fast–traveling tsunamis driven by atmospheric Lamb waves on the 2022 Tonga eruption. *Science*. doi:10.1126/science.abo4364

Kusky, T. M. (2022). Déjà vu: Might Future Eruptions of Hunga Tonga-Hunga Ha'apai Volcano be a Repeat of the Devastating Eruption of Santorini, Greece (1650 BC)? *Journal of Earth Science, 33(2),* 229-235. doi:10.1007/s12583-022-1624-2

Larkina, v. I., Nalivayko, A. V., Gokhberg, M. B., Liperovskiy, V. A., and Shalimov, S. L. (1983). Observation of VLF emission related with seismic activity on the Intercosmos–19 satellite. *Geomagnetism and Aeronomy*, *23*(5), 684–687.

Liu, J. Y., Chuo, Y. J., Shan, S. J., Tsai, Y. B., Chen, Y. I., Pulinets, S. A., and Yu, S. B. (2004). Pre–earthquake ionospheric anomalies registered by continuous GPS TEC measuremants. *Annales Geophysicae*, 22: 1585–1593. doi:1432–0576/ag/2004–22–1585

Le, H., Liu, J. Y., and Liu, L. (2011). A statistical analysis of ionospheric anomalies before 736M6.0+ earthquakes during 2002–2010. *Journal of Geophysical Research: Space Physics, 116*(A2), n/a–n/a. doi:10.1029/2010ja015781

Leonard, R. S., and Barnes, R. A., Jr (1965). Observation of ionospheric disturbances following the Alaska earthquake. *Journal of Geophysical Research, 70*(5),1250–1253.

Li, W., Guo, J., Yue, J., Shen, Y., and Yang, Y. (2016). Total electron content anomalies associated with global VEI4 + volcanic eruptions during 2002–2015. *Journal of Volcanology and Geothermal Research, 325*, 98–109. doi:10.1016/j.jvolgeores.2016.06.017

Lin, J.–W. (2017). Ionospheric Anomaly due to the volcanic eruption in Colima, Mexico, 06 January 2013: Two–Dimensional Principal Component Analysis. *European Journal of Remote Sensing, 46*(1), 689–698. doi:10.5721/EuJRS20134640

Lin, J.–T., Rajesh, P. K., Lin, C. C. H., Chou, M.–Y., Liu, J.–Y., Yue, J., Hsiao T.–Y., Tsai, H.–F., Chao, H.–M., . . . Kung, M. M. (2022). Rapid Conjugate Appearance of the Giant Ionospheric Lamb Wave Signatures in the Northern Hemisphere After Hunga–Tonga Volcano Eruptions. *Geophysical Research Letters, 49*(8). doi:10.1029/2022gl098222

Liu, J., Wan, W. X., Huang, J. P., Zhang, X. M., Zhao, S. F., Ouyang, X. Y., and Zeren, Z.–M. (2011). Electron Density Perturbation befero Chile M8.8 Earthquake. *Chinese J. Geophys.* (in Chinese), *54*(11), 2717–2725. doi:10.3969/j.issn.0001–5733.2011.11.001

Liu, J. Y., Chen, Y. I., Chuo, Y. J., and Chen, C. S. (2006a). A statistical investigation of preearthquake ionospheric anomaly. *Journal of Geophysical Research, 111*(A5). doi:10.1029/2005ja011333

Liu, J. Y., Chen, Y. I., Pulinets, S. A., Tsai, Y. B., and Chuo, Y. J. (2000). Seismo–ionospheric signatures prior to M ≥6.0 Taiwan earthquakes. *Geophysical Research Letters, 27*(19), 3113–3116. doi:10.1029/2000gl011395

Liu, J. Y., Tsai, Y. B., Chen, S. W., Lee, C. P., Chen, Y. C., Yen, H. Y., Chang, W. Y., . . . Liu, C. (2006b). Giant ionospheric disturbances excited by the M9.3 Sumatra earthquake of 26 December 2004. *Geophysical Research Letters, 33*(2). doi:10.1029/2005gl023963

Liu, X., Xu, J., Yue, J., and Kogure, M. (2022). Strong Gravity Waves Associated With Tonga Volcano Eruption Revealed by SABER Observations. *Geophysical Research Letters, 49*(10). doi:10.1029/2022gl098339

Liu, X., Zhang, Q., Shah, M., and Hong, Z. (2017). Atmospheric–ionospheric disturbances following the April 2015 Calbuco volcano from GPS and OMI observations. *Advances in Space Research, 60*(12), 2836–2846. doi:10.1016/j.asr.2017.07.007

Lockner, D. A., Johnston, M. J. S., and Byerlee, J. D. (1983). A mechanism to explain the generation of earthquake lights, *Nature*, *302*(3), 28–33. doi:10.1038/302028a0

Maletckii, B., & Astafyeva, E. (2022). Near‐Real‐Time Analysis of the Ionospheric Response to the 15 January 2022 Hunga Tonga‐Hunga Ha'apai Volcanic Eruption. *Journal of Geophysical Research: Space Physics, 127*(10). doi:10.1029/2022ja030735

Manta, F., Occhipinti, G., Hill, E. M., Perttu, A., Assink, J., and Taisne, B. (2021). Correlation Between GNSS–TEC and Eruption Magnitude Supports the Use of Ionospheric Sensing to Complement Volcanic Hazard Assessment. *Journal of Geophysical Research: Solid Earth, 126*(2). doi:10.1029/2020jb020726

Meridian. (2022). Ground–based Spsce Environment Monitoring Network. Retrieved from http://www.meridianproject.ac.cn/en_home.html

Matoza, R. S., Fee, D., Assink, J. D., Iezzi, A. M., Green, D. N., Kim, K., Wilson, D. C. (2022). Atmospheric waves and global seismoacoustic observations of the January 2022 Hunga eruption, Tonga. *Science*. doi:10.1126/science.abo7063

Nakashima, Y., Heki, K., Takeo, A., Cahyadi, M. N., Aditiya, A., and Yoshizawa, K. (2016). Atmospheric resonant oscillations by the 2014 eruption of the Kelud volcano, Indonesia, observed with the ionospheric total electron contents and seismic signals. *Earth and Planetary Science Letters, 434*, 112–116. doi:10.1016/j.epsl.2015.11.029

NASA. (2022). Hunga Tonga–Hunga Ha‘apai Erupts. Retrieved from https://earthobservatory.nasa.gov/images/149347/hunga–tonga–hunga–haapai–erupts

NPR. (2022). NASA scientists estimate Tonga blast at 10 megatons. Retrieved from https://www.npr.org/2022/01/18/1073800454/nasa–scientists–estimate–tonga–blast–at–10–megatons

Pandara, D. P., Muslim, B., Sunardi, B., Ferdy, Pasau, G., Mananohas, M., and Ango, C. (2021). Analysis of Ionosphere disturbance caused by the Lokon Volcano Eruption using GPS TEC data. *IOP Conference Series: Materials Science and Engineering, 1115*(1), 012062. doi:10.1088/1757–899x/1115/1/012062

Pan, S.-Y., Hsieh, B.-Z., Lu, M.-T., & Lin, Z.-S. (2008). Identification of stratigraphic formation interfaces using wavelet and Fourier transforms. *Computers & Geosciences, 34*(1), 77-92. doi:10.1016/j.cageo.2007.01.002

Parrot, M., Benoist, D., Berthelier, J. J., Błęcki, J., Chapuis, Y., Colin, F., Elie, F., Fergeau, P., Lagoutte, D., Lefeuvre, F., Le´veˆquea, M., Pinc–on, J. L.,Poirier, B., Seran, H.–C., . . . Zamora, P. (2006a). The magnetic field experiment IMSC and its data processing onboard DEMETER: Scientific objectives, description and first results. *Planetary and Space Science, 54*(5), 441–455. doi:10.1016/j.pss.2005.10.015

Parrot, M., Berthelier, J. J., Lebreton, J. P., Sauvaud, J. A., Santolik, O., and Blecki, J. (2006b). Examples of unusual ionospheric observations made by the DEMETER satellite over seismic regions. *Physics and Chemistry of the Earth, Parts A/B/C, 31*(4–9), 486–495. doi:10.1016/j.pce.2006.02.011

Poli, P., and Shapiro, N. M. (2022). Rapid Characterization of Large Volcanic Eruptions: Measuring the Impulse of the Hunga Tonga Ha’apai Explosion From Teleseismic Waves. *Geophysical Research Letters, 49*(8). doi:10.1029/2022gl098123

Proud, S.R., Prata, A.T., and Schmauss, S. (2022). The January 2022 eruption of Hunga Tonga-Hunga Ha'apai volcanoe reached the mesophere. *Science, 378*, 554-557 doi:10.1126/science.abo4076

Pulinets, S. A., Liu, J. Y., and Safronova, I. A. (2004). Interpretation of a Statistical analysis of variations in the foF2 critical frequency before earthquakes based on data from Chung–Li ionospheric station. *Geomagnetism and Aeronomy*, *44*(1), 102–106. doi:10.1016/S0016–7037(03)00446–0

Qian, L., Marsh, D., Merkel, A., Solomon, S. C., & Roble, R. G. (2013). Effect of trends of middle atmosphere gases on the mesosphere and thermosphere. *Journal of Geophysical Research: Space Physics, 118*(6), 3846-3855. doi:10.1002/jgra.50354

Ricardo Garza-Girón, T. L., Frederick Pollitz, Hiroo Kanamori, Luis Rivera. (2023). Solid Earth–atmosphere interaction forces during the 15 January 2022 Tonga eruption. *SCIENCE ADVANCES, 9*(15). doi:10.1126/sciadv.add4931

Roble, R. G., & Dickinson, R. E. (1989). How will changes in carbon dioxide and methane modify the mean structure of the mesosphere and thermosphere? *Geophysical Research Letters, 16*(12), 1441-1444. doi:10.1029/GL016i012p01441

Saito, S. (2022). Ionospheric disturbances observed over Japan following the eruption of Hunga Tonga–Hunga Ha'apai on 15 January 2022. *Earth, Planets and Space, 74*(1). doi:10.1186/s40623–022–01619–0

Satti, M. S., Ehsan, M., Abbas, A., Shah, M., de Oliveira–Júnior, Jos´e, J. F., and Naqvi, N. A. (2022). Atmospheric and ionospheric precursors associated with M $\geq$ 6.5 earthquakes from multiple satellites. *Journal of Atmospheric and Solar–Terrestrial Physics, 227*, 105802. doi:10.1016/j.jastp.2021.105802

SEPC. (2022a). Space Environment Prediction Center: 3 Hour Kp Forecast. Retrieved from http://www.sepc.ac.cn/Kp3HPred_chn.php

SEPC. (2022b). Space Environment Prediction Center: Event Alerts-geomagnetic storm. Retrieved from http://www.sepc.ac.cn/GMS_chn.php

Sigurdsson, H., Houghton, B., McNutt, S., Rymer, H., & Stix, J. (2015). *The encyclopedia of volcanoes* (H. Sigurdsson, B. Houghton, S. McNutt, H. Rymer, & J. Stix Eds. 2 ed.): Elsevier.

Shults, K., Astafyeva, E., and Adourian, S. (2016). Ionospheric detection and localization of volcano eruptions on the example of the April 2015 Calbuco events. *Journal of Geophysical Research: Space Physics, 121*(10). doi:10.1002/2016ja023382

Toman, I., Brčić, D., and Kos, S. (2021). Contribution to the Research of the Effects of Etna Volcano Activity on the Features of the Ionospheric Total Electron Content Behaviour. *Remote Sensing, 13*(5), 1006. doi:10.3390/rs13051006

Toman, K. (1966). Fourier Transform of the Sunspot Cycle. *Journal of Geophysical Research, 71*(13), 3285-3286.

UNISDR. (2015). The Human Cost Of Natural Disasters: A global perspective.

Velasco Herrera, V. M., Rossello E. A., Orgeira, M. J., Arioni, L., Soon, W., Velasco. G., Rosique-de la Cruz, L., Zúñiga, E. and Vera, C. (2022). Long-Term Forecasting of Strong Earthquakes in North America, South America, Japan, Southern China and Northern India With Machine Learning. *Front. Earth Sci.* 10:905792. doi: 10.3389/feart.2022.905792

Verhulst, T. G. W., Altadill, D., Barta, V., Belehaki, A., Burešová, D., Cesaroni, C., Galkin, I., Guerra, M., Ippolito, A., Herekakis, T., Kouba, D., Mielich, J., Segarra, A., Spogli, L., Tsagouri, I. (2022). Multi-instrument detection in Europe of ionospheric disturbances caused by the 15 January 2022 eruption of the Hunga volcano. *Journal of Space Weather and Space Climate, 12*. doi:10.1051/swsc/2022032

Vladimir Troyan, & Yurii Kiselev. (2010). Statistical Methods of Geophysical Data Processing: *World Scientific Publishing Company.*

Wang, C., and Wei, F. S. (2007). *The Introduction of Meridian Project.* Paper presented at the The 23rd Annual Meeting of Chinese Geophysical Society, Qingdao, Shandong, China.

Watson, L. M., Iezzi, A. M., Toney, L., Maher, S. P., Fee, D., McKee, K., . . . Johnson, J. B. (2022). Volcano infrasound: progress and future directions. *Bulletin of Volcanology, 84*(5). doi:10.1007/s00445–022–01544–w

Wright, C. J., Hindley, N. P., Alexander, M. J., Barlow, M., Hoffmann, L., Mitchell, C. N., . . . Yue, J. (2022). Tonga eruption triggered waves propagating globally from surface to edge of space. doi:10.1002/essoar.10510674.1

Zhang, X. M., J. Liu, J.D. Qian, X. Y. Ouyang, X. H. Shen, S. F. Zhao. (2008). Ionospheric electromagnetic disturbance before Gaize earthquake with MS 6.9 Tibet. *Earthquake*, 28(3), 14–22.

Zhang, S.–R., Vierinen, J., Aa, E., Goncharenko, L. P., Erickson, P. J., Rideout, W., Coster, A. J., . . . Spicher, A. (2022). 2022 Tonga Volcanic Eruption Induced Global Propagation of Ionospheric Disturbances via Lamb Waves. *Frontiers in Astronomy and Space Sciences, 9*. doi:10.3389/fspas.2022.871275

Zhang, X. M., Qian, J. D., Ouyang, X. Y., Cai, J. A., Liu, J., Shen, X. H., & Zhao, S. F. (2009). Ionospheric Electro–magnetic Disturbances Prior to Yutian 7.2 Earthquake in Xinjiang. *Chin. J. Space Sci.*, *29*(2), 213–221.

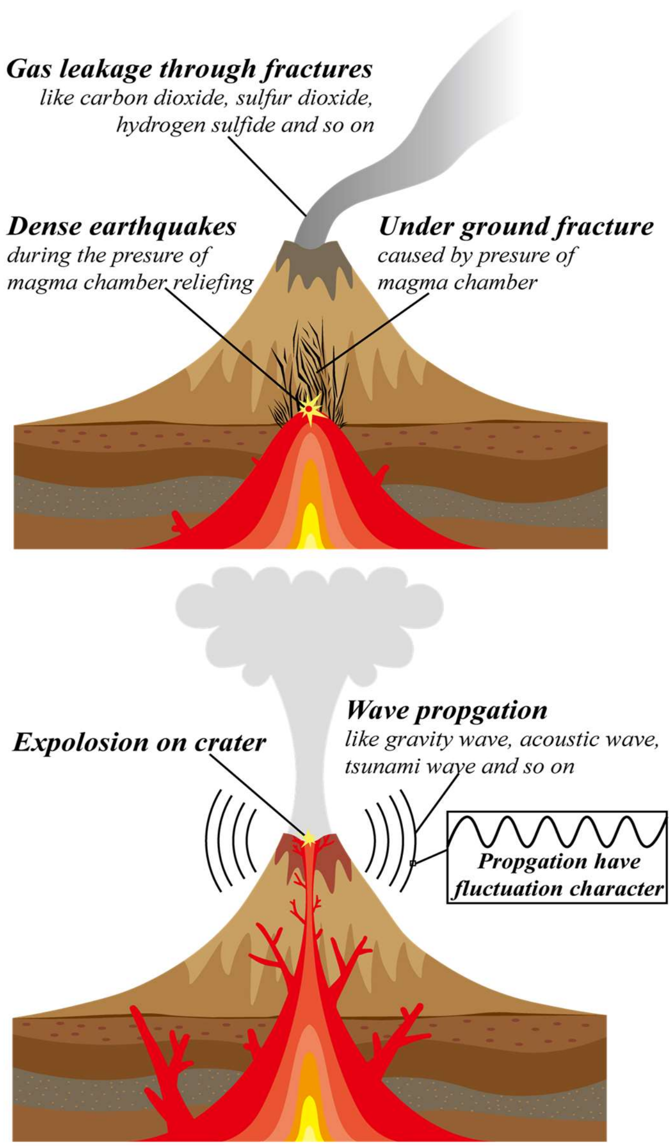

Figure 1. Schematic diagram of volcanic-related processes during the pre-eruption and eruption phases. The upper (top) figure is for the pre-eruption phase, and the lower (bottom) figure is for the eruption phase. In this study, we assume that the pre-eruption phase will trigger dense earthquakes and cause the release of significant amounts of gas from magma capsule as the sketch is indicating. These processes will change the composition over local atmosphere and generate both gravity wave and seismic wave, and they will further affect the ionosphere [*Sigurdsson et al.*, 2015]. We believe that there are a variety of gases dissolved in magma capsule like carbon dioxide (CO_2), sulfur dioxide (SO_2), hydrogen sulfide (H_2S), carbon monoxide (CO), hydrogen chloride (HCl) and so on [*Sigurdsson et al.*, 2015]. We think there are enough studies to prove that these gases which leak from underground fissure at pre-eruption period can change the temperature of upper atmosphere and lower the electron density [*Cnossen*, 2022; *Qian et al.*, 2013; *Roble & Dickinson*, 1989]. In the meantime, the volcanic eruption phase will generate much more gravity wave, seismic wave, acoustic wave and infrasonic wave [*Ricardo Garza-Girón*, 2023]. Although this effect

is not global and has low strength, the local variation will propagate outward by the dynamic action of the upper atmosphere.

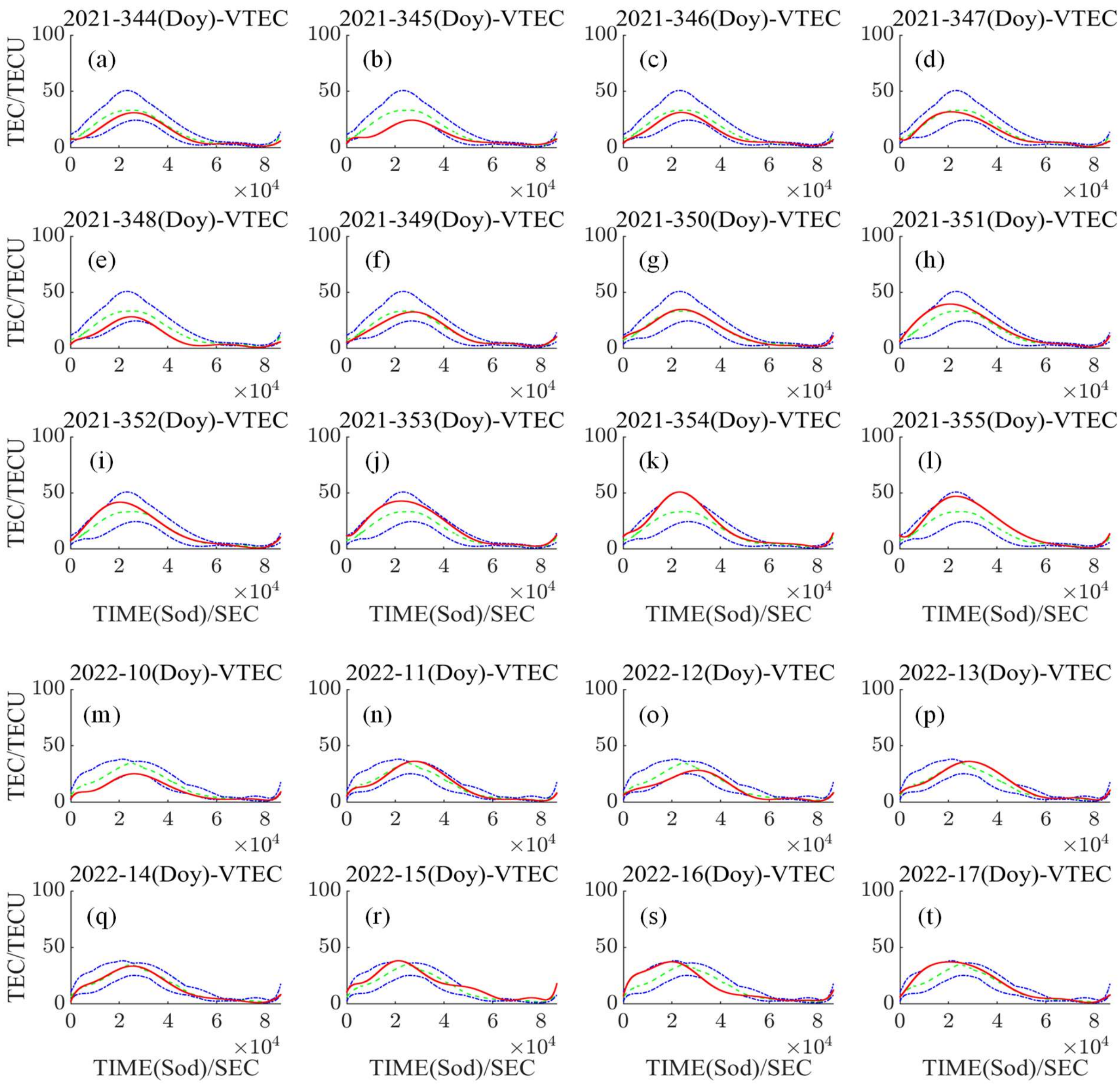

Figure 2. Plot of ionospheric TEC values over Sanya station, Hainan, during the volcanic eruption. The green dashed lines point out the median values for the time period, the blue dashed lines indicate the maximum and minor values, and the red solid lines mark the fitted value over the station. (a–l): TEC variation during December 10–21, 2021 (Doy344–Doy355). It can be found that on December 20th, at the beginning of Doy354, the fitted value deviates significantly from the median value, and the TEC fluctuates distinctly. The maximum peak reaches 50 TECU, which is higher than the daily maximum peak of about 20–30 TECU. (m–t): The TEC variation from 10 to 17 January 2022 (Doy10–Doy17). It can be found that there are fluctuations in ionosphere 15 TEC, but the overall anomaly is smaller than that in (a–l).\

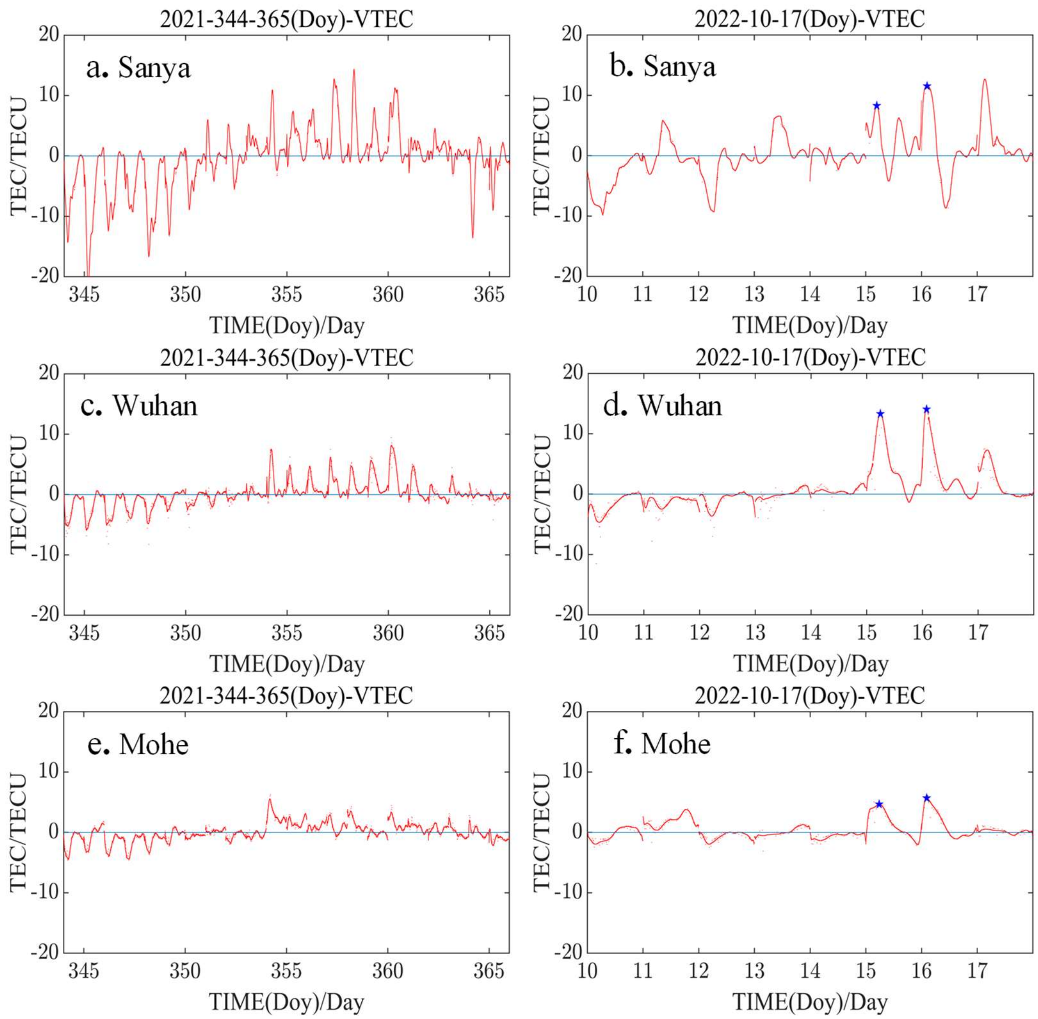

Figure 3. The TEC anomalies over Sanya, Wuhan and Mohe stations during the eruption phase. The red solid line is the interpolation of the fitting value, and the blue horizontal line indicates the zero level of TECU. The blue asterisk is the maximal value of the similar waveform selected. (a): Anomalies during the period from December 10 to 31, 2021 (Doy344–Doy365) over Sanya station. (b): Plot of anomalous variation from January 10 to 17, 2022 (Doy10–Doy17) over Sanya station. (c): Anomalies during the period from December 10 to 31, 2021 (Doy344–Doy365) over Wuhan Zuoling station. (d): Plot of anomalous variation from January 10 to 17, 2022 (Doy10–Doy17) over Wuhan Zuoling station. (e): Anomalies during the period from December 10 to 31, 2021 (Doy344–Doy365) over Mohe station. (f): Plot of anomalous variation from January 10 to 17, 2022 (Doy10–Doy17) over Mohe station. The TEC decays substantially from 10 days before the 20th (Doy354), and the anomalous variations exhibit significant increase with oscillations before the outbreak on the 20th. Similar decay can be found in several days before the outbreak on 13th, but the overall amplitude is smaller than that of (a, c, and e). After decaying, TEC anomalies appear to undergo significant enhancement on the Doy354 and Doy15, respectively. Here is the difference: there are many peaks with different shapes and intensities during the intermittent stage. However, the anomalies variation in main stage has similar distinct waveform characteristic and relatively close intensity.

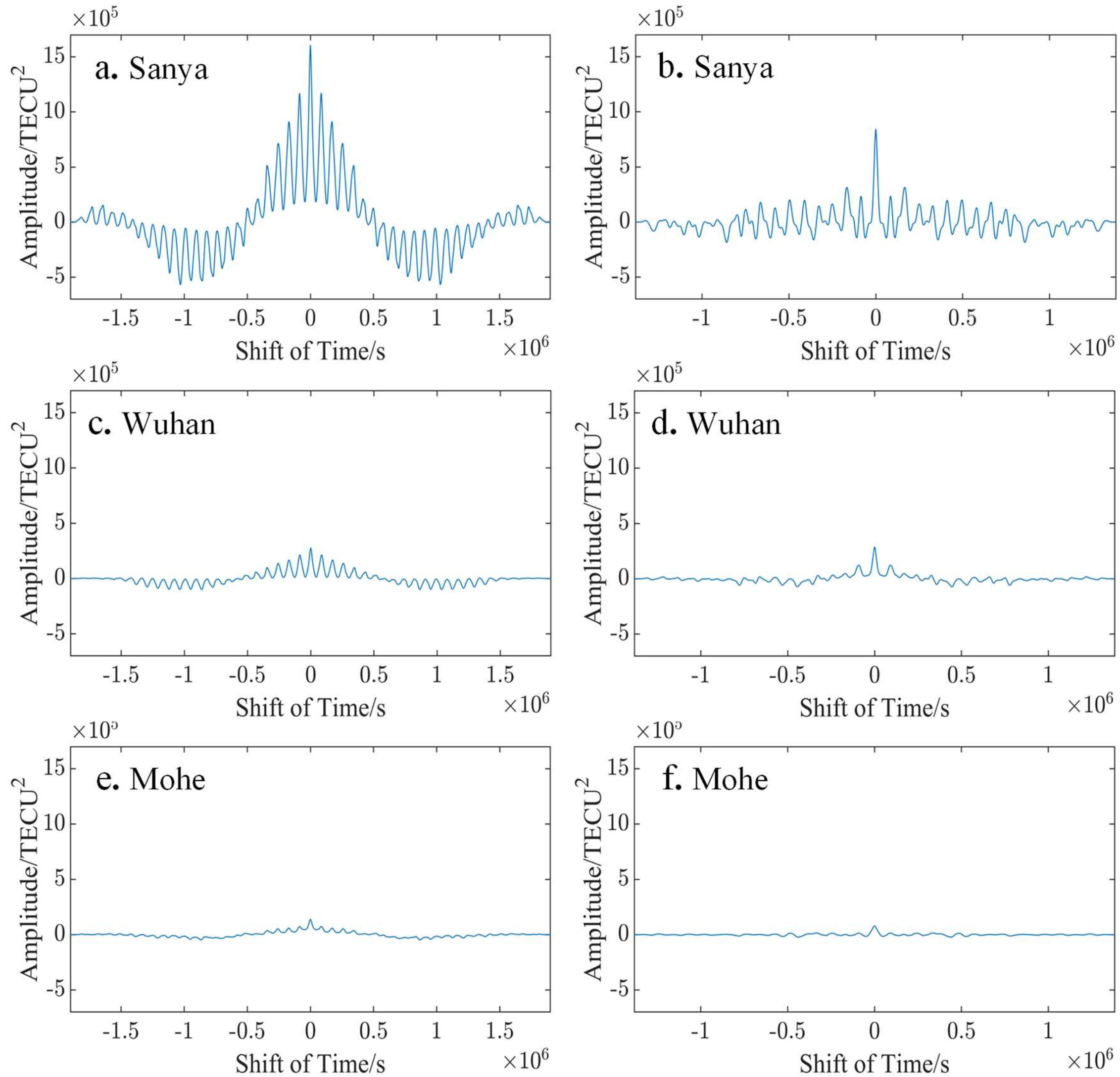

Figure 4. Autocorrelation results of anomalous variations during the eruption. The horizontal coordinates are the time–shift taken by the autocorrelation function. (a): The autocorrelation of the intermittent stage over Sanya shows that the maximum peak value of the autocorrelation function is not prominent. (b): It can be found that the maximum peak of autocorrelation function is 4–10 times higher than other smaller peaks during the main stage over Sanya. (c): The result of autocorrelation analysis of the TEC anomaly during the intermittent stage over Wuhan Zuoling station. Its signal attenuation degree is between that over Sanya and Mohe, with similar change pattern. (d): The plot of autocorrelation analysis over Wuhan Zuoling station during the main stage. (e): The plot of autocorrelation analysis of the intermittent stage over Mohe station. The the attenuation of the signal intensity is shown obviously, with similar variation characteristics as Sanya. (f): The result of autocorrelation of the main stage over Mohe. By demonstrating a clear ionospheric response to eruptions in this study, we can reduce the noise and increase the peak value through autocorrelation. After autocorrelating, each peak of the result may show a peak of TEC anomalies for one eruption. We can get an approximate number of eruptions by this method. Our work may be able to provide a kind of corroboration for volcanic research in such data-missing case.

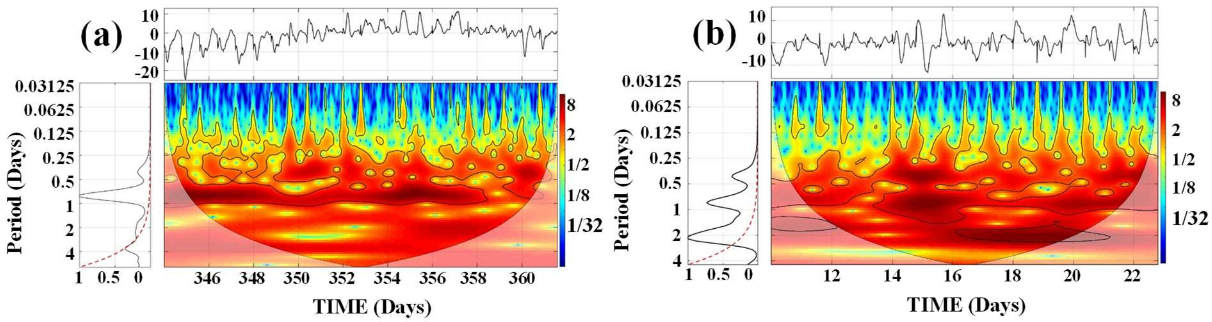

Figure 5. The plot through the Wavelet analysis of the anomalies. (a): The result of wavelet analysis of the TEC anomaly over Sanya during the intermittent stage. (b): The result of wavelet analysis of the TEC anomaly over Sanya during the main stage. For (a) and (b), the upper panels show the results of the low-frequent component of the signals. The lower panels exhibit the continuous wavelet transform time-frequency diagram without the edge effect. The left panels reveal the signal period extracted through wavelet transform.

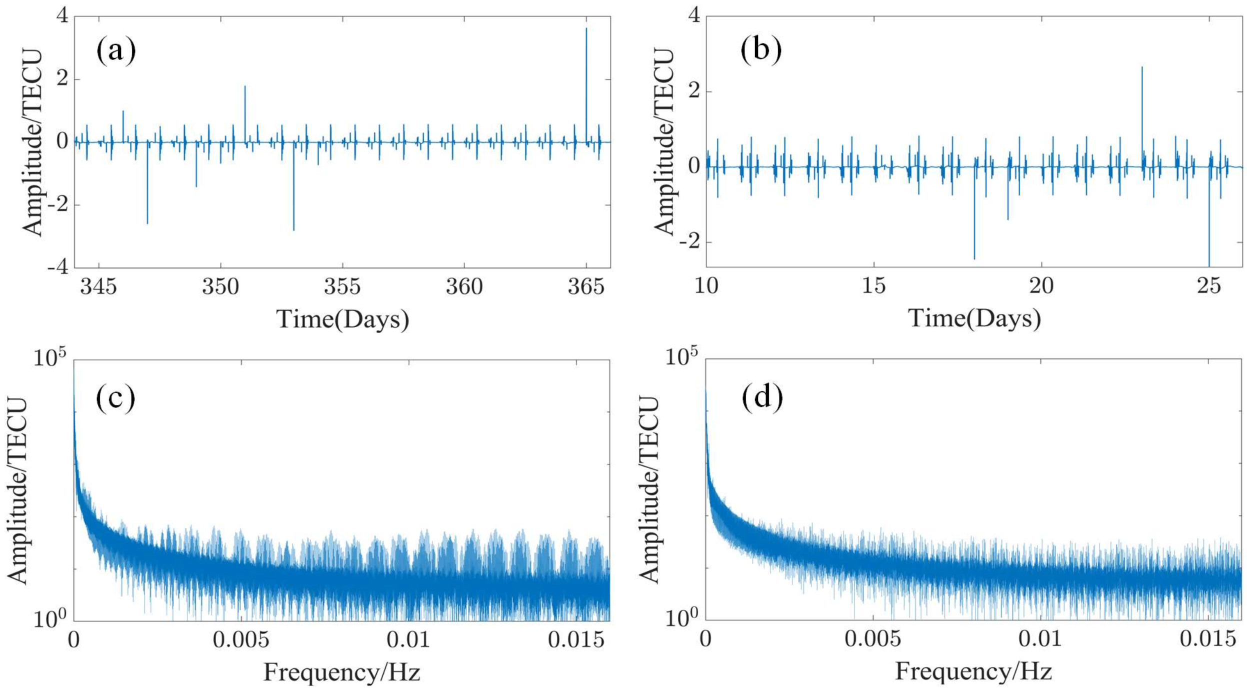

Figure 6. The supplementary plots based on the Fourier analysis of the anomalies. (a): High-frequency part of the discrete wavelet transform of the TEC abnormal signals over Sanya during the intermittent phase. (b): High-frequencies part over Sanya during the main outburst phase. (c): During December 10–21, 2021 (Doy344–Doy355), the energy is mainly concentrated in the frequency range of an order of $0 - 10^{-3}$ Hz over Sanya. (d): The amplitude spectrum from 10 to 17 January 2022 (Doy10–Doy17) over Sanya. It can be discerned that the energy is mainly concentrated in $0 - 10^{-3}$Hz.